

RECURRENT RADIO OUTBURSTS AT THE CENTER OF THE NGC 1407 GALAXY GROUP

SIMONA GIACINTUCCI^{1,2}, EWAN O’SULLIVAN³, TRACY E. CLARKE⁴, MATTEO MURGIA⁵, JAN M. VRTILEK³, TIZIANA VENTURI⁶,
LAURENCE P. DAVID³, SOMAK RAYCHAUDHURY⁷, RAMANA M. ATHREYA⁸

The Astrophysical Journal, *accepted on 2012 June 23*

ABSTRACT

We present deep *Giant Metrewave Radio Telescope (GMRT)* radio observations at 240, 330 and 610 MHz of the complex radio source at the center of the NGC1407 galaxy group. Previous *GMRT* observations at 240 MHz revealed faint, diffuse emission enclosing the central twin-jet radio galaxy. This has been interpreted as an indication of two possible radio outbursts occurring at different times. Both the inner double and diffuse component are detected in the new *GMRT* images at high levels of significance. Combining the *GMRT* observations with archival *Very Large Array* data at 1.4 and 4.9 GHz, we derive the total spectrum of both components. The inner double has a spectral index $\alpha = 0.7$, typical for active, extended radio galaxies, whereas the spectrum of the large-scale emission is very steep, with $\alpha = 1.8$ between 240 MHz and 1.4 GHz. The radiative age of the large-scale component is very long, ~ 300 Myr, compared to ~ 30 Myr estimated for the central double, confirming that the diffuse component was generated during a former cycle of activity of the central galaxy. The current activity have so far released an energy which is nearly one order of magnitude lower than that associated with the former outburst. The group X-ray emission in the *Chandra* and *XMM-Newton* images and extended radio emission show a similar swept-back morphology. We speculate that the two structures are both affected by the motion of the group core, perhaps due to the core sloshing in response to a recent encounter with the nearby elliptical galaxy NGC 1400.

Subject headings: galaxies: clusters: general — galaxies: individual (NGC1407) — intergalactic medium — radio continuum: galaxies — X-rays: galaxies: clusters

1. INTRODUCTION

Quoting Lara et al. (1999), “*radio sources are born, grow and finally ... sleep*”. The dormant phase in the evolutionary course of a radio galaxy and fate of the radio-emitting plasma after the cessation of the nuclear activity are among the most intriguing issues in extragalactic astronomy. The active stage of a powerful radio source, typically associated with an elliptical galaxy, can last several 10^7 up to few 10^8 years. During this time, the radio galaxy is likely fed by mass accretion onto the supermassive black hole of the host galaxy. Once this accretion is interrupted, or becomes insufficient to support radio activity, the radio source enters a dying phase (e.g., Murgia et al. 2011, and references therein); the radio emission passively evolves and rapidly fades, even if expansion losses are negligible and the relativistic electrons are subject only to radiative losses. This is reflected into a pronounced steepening of the integrated radio spectrum whose slope α can reach ultra-steep values, $\alpha \gtrsim 2$ (e.g., Komissarov & Gubanov 1994), adopting the convention $S_\nu \propto \nu^{-\alpha}$ for the synchrotron spectrum, where S_ν is the flux density at the frequency ν . Eventually, the radio

emission disappears below the detection limit of present radio telescopes.

During the fading stage of a radio source, the central nucleus may switch on again and produce new radio activity, thus leading to a restarted radio source. Evidence for episodic radio activities are reported in the literature for a growing number of radio galaxies (see, for instance, Saikia & Jamrozy 2009 for a review). Double-double radio galaxies (Schoenmakers et al. 2000) qualify as one of the most unmistakable examples of recurrent nuclear activity; here a new pair of inner lobes are produced close to the nucleus before the previously generated, more distant ones have completely faded (e.g., Subrahmanyam et al. 1996; Lara et al. 1999; Saikia & Jamrozy 2009). Another type of restarted radio sources are “nesting” radio galaxies (Jamrozy et al. 2007), i.e., sources characterized by a faint, extended structure, within which a bright radio source, extended on a significantly smaller scale, is embedded. Examples are Hercules A (Gizani & Leahy 2003; Gizani et al. 2005), 3C 310 (van Breugel & Fomalont 1984; Leahy et al. 1986), and 4C 29.30 (Jamrozy et al. 2007). In few well-studied cases, the large-scale emission and inner source appear clearly, and quite sharply, separated in the spectral index distribution (e.g., Gizani & Leahy 2003), with much steeper spectral index values measured for the outer emission. This has been interpreted as evidence for different epochs of jet activity, with the more extended and steeper component being related to an earlier outburst of the central active galactic nucleus (AGN).

In this paper, we focus on the complex radio source associated with the elliptical galaxy NGC 1407 (see Table 1), at the center of the poor group of galaxies Eridanus A at $z=0.0059$, with a one-dimensional velocity dispersion $\sigma_v = 372$ km s⁻¹ (Brough et al. 2006) and 0.3-2 keV X-ray luminosity of $10^{41.7}$ erg s⁻¹ (Forbes et al. 2006). Based on *Giant Metrewave Radio*

¹ Department of Astronomy, University of Maryland, College Park, MD 20742, USA; simona@astro.umd.edu

² Joint Space-Science Institute, University of Maryland, College Park, MD, 20742-2421, USA

³ Harvard-Smithsonian Center for Astrophysics, 60 Garden Street, Cambridge, MA 02138, USA

⁴ Naval Research Laboratory, Code 7213, Washington, DC 20375, USA

⁵ INAF-Osservatorio Astronomico di Cagliari, Loc. Poggio dei Pini, Strada 54, I-09012 Capoterra (CA), Italy

⁶ INAF - Istituto di Radioastronomia, via Gobetti 101, I-40129 Bologna, Italy

⁷ School of Physics and Astronomy, University of Birmingham, Birmingham, B15 2TT, UK

⁸ Indian Institute of Science Education and Research, Central Tower, Sai Trinity Building, Sutarwadi Road, Pashan, Pune 411021, India

TABLE 1
GENERAL PROPERTIES OF NGC 1407

| | |
|------------------------------|------------|
| RA _{J2000} (h m s) | 03 40 11.9 |
| DEC _{J2000} (° ′ ″) | −18 34 39 |
| z | 0.0059 |
| D_L (Mpc) | 25.0 |
| angular scale (kpc/″) | 0.120 |
| morphology | E0 |
| M_R (mag) | −22.8 |

Notes to Table 1 – RA_{J2000} and DEC_{J2000} are the coordinates of the optical galaxy from the NASA/IPAC Extragalactic Database (NED). The optical redshift z is from Quintana et al. (1994). The galaxy morphological classification is from the Third Reference Catalogue of Bright Galaxies (De Vaucouleurs et al. 1991). The Cousins R-band absolute magnitude is from Trentham et al. (2006). We assume a flat cosmology with $H_0 = 71 \text{ km s}^{-1} \text{ Mpc}^{-1}$, $\Omega_\lambda = 0.73$ and $\Omega_0 = 0.27$.

Telescope (*GMRT*) observations at 240 MHz and 610 MHz, Giacintucci et al. (2011, hereinafter G11) suggested that this source may be a restarted radio galaxy. Here, we present a multifrequency radio study of NGC 1407 based on new, deep *GMRT* observations at 240 MHz, 330 MHz and 610 MHz, and multifrequency data from the *Very Large Array* (*VLA*) archive. Our study is complemented with the analysis of *Chandra* and *XMM-Newton* X-ray data.

2. RADIO OBSERVATIONS

In this section, we present the new *GMRT* observations of NGC 1407 at 240 MHz, 330 MHz and 610 MHz. Details on these observations are summarized in Table 2 which reports: observing date, frequency and total bandwidth in columns 1, 2 and 3; total time on source (column 4); full-width half maximum (FWHM) and position angle (PA) of the full array (column 5); rms level (1σ) at full resolution (column 6).

The *GMRT* data were supplemented by all useful observations in the *VLA* archive. The observing details are provided in Table 3, which shows the project code and array configuration in the first two columns; the other columns provide the same information as Table 2.

2.1. GMRT observations

NGC 1407 was observed with the *GMRT* at 240 MHz, 330 MHz and 610 MHz (project 17_034; Table 2) in a full-synthesis run of approximately 9 hours (including calibration overheads) at each frequency. The observations at 240 MHz and 610 MHz were made using the dual-frequency mode, recording LL polarization at 240 MHz and RR polarization at 610 MHz. Both RR and LL were recorded at 330 MHz.

The 330 MHz and 610 MHz data were collected using the upper and lower side bands simultaneously (USB and LSB, respectively), for a total observing bandwidth of 32 MHz. Only the USB was used at 240 MHz, with 8 MHz bandwidth. The default spectral-line observing mode was used, with 128 channels for each band (64 channel at 240 MHz) and a spectral resolution of 125 kHz/channel. The datasets were calibrated and reduced using the NRAO Astronomical Image Processing System package (AIPS). We refer to Giacintucci et al. (2008, 2011) for a description of the data reduction.

Self-calibration was applied to reduce residual phase variations and improve the quality of the final images. Due to the large field of view of the *GMRT* at all frequencies, we used

the wide-field imaging technique at each step of the phase self-calibration process, to account for the non-planar nature of the sky. The final images were produced using the multi-scale CLEAN implemented in the AIPS task IMAGR, which results in better imaging of extended sources compared to the traditional CLEAN (e.g., Clarke & Enns 2006, for a detailed discussion, see Appendix A in Greisen et al. (2009)). We used delta functions as model components for the unresolved features and circular Gaussians for the resolved ones, with increasing width to progressively highlight the extended emission during the clean. Beyond the image at full resolution (Table 2), we produced images with lower resolution (down to $\sim 45''$), tapering the uv data by means of the parameters ROBUST and UVTAPER in IMAGR. The final images were corrected for the *GMRT* primary beam response using the task PBCOR in AIPS. The rms noise level (1σ) achieved in the final images at full resolution is given in Table 2.

We adopted the scale of Baars et al. (1977) for the flux density calibration. Residual amplitude errors are within 8% at 240 MHz and 330 MHz, and 5% at 610 MHz (Chandra et al. 2004).

2.2. VLA archive data

We extracted and reduced *VLA* archive data of NGC 1407 at 327 MHz, 1.4 GHz and 4.9 GHz (see Table 3 for details). The observations were all pointed on NGC 1407, excepting those at 4.9 GHz in BnC configuration, where the phase center is 6' south-west of the galaxy.

The observations at 327 MHz were obtained in multi-channel continuum mode with 16 channels and a total bandwidth of 6.3 MHz. The dataset was calibrated using 3C48 as bandpass and amplitude calibrator. Due to problems with the source observed as phase calibrator (0340-213), 3C48 was also used for the phase calibration.

All data were processed in AIPS and images were produced using the standard Fourier transform deconvolution method. Self-calibration was applied to reduce the effects of residual phase errors in the data. Due to the large field of view at 327 MHz, the wide-field imaging technique was implemented to correct for distortions in the image caused by the non-coplanarity of the *VLA*. Correction for the primary beam attenuation was applied to the final images at all frequencies using the task PBCOR in AIPS. All flux densities are on the Baars et al. (1977) scale and average residual amplitude errors are $\lesssim 5\%$.

3. THE RADIO IMAGES

The *GMRT* 330 MHz image at full resolution ($\sim 12''$) is presented in Fig. 1a, overlaid on the optical image from The Second Palomar Sky Survey (POSS 2). Faint, diffuse emission (white contours) is detected around the central double source S3 (magenta contours), in good agreement with the 240 MHz image in G11 (also shown in Fig. 8). S1, S2 and S4 are discrete radio sources located, in projection, within the diffuse emission. S1 and S2 have no optical counterpart on the POSS-2 image, while a very faint object seems to be associated with S4, suggesting that all three sources are background radio galaxies.

Hereinafter, we will refer to the two components of the NGC 1407 system as the inner double and large-scale emission.

3.1. The inner double

TABLE 2
 DETAILS OF THE *GMRT* OBSERVATIONS.

| Observation date | ν (MHz) | $\Delta\nu$ (MHz) | t (min) | FWHM, p.a. ($'' \times ''$, $^\circ$) | rms (mJy beam $^{-1}$) |
|------------------|------------------|-------------------|---------|--|-------------------------|
| Nov 19, 2009 | 240 ^a | 8 | 270 | 16.1 \times 10.9, 36 | 0.25 |
| Jan 17, 2010 | 330 | 32 | 330 | 12.1 \times 9.2, 42 | 0.16 |
| Nov 19, 2009 | 610 ^a | 32 | 270 | 8.2 \times 4.4, 46 | 0.05 |

Notes to Table 2 – *a*: observed in simultaneous 240 MHz/610 MHz mode.

 TABLE 3
 DETAILS OF THE *VLA* ARCHIVE OBSERVATIONS.

| Project code | Array | Observation date | ν (MHz) | $\Delta\nu$ (MHz) | t (min) | FWHM, p.a. ($'' \times ''$, $^\circ$) | rms (mJy beam $^{-1}$) |
|--------------|-------|------------------|-------------|-------------------|---------|--|-------------------------|
| AS827 | B | Apr 30, 2005 | 322/329 | 6.3 | 130 | 27.7 \times 17.0, -16 | 3 |
| AV151 | A | July 3, 1987 | 1446/1496 | 12.5 | 3 | 2.2 \times 1.3, 11 | 0.1 |
| AR536 | CD | May 28, 2004 | 1385/1465 | 50 | 20 | 76.2 \times 20.8, 54 | 0.08 |
| AW136 | BC | Jun 23, 1985 | 4835/4885 | 50 | 6.5 | 5.1 \times 2.0, 71 | 0.14 |
| AW112 | C | Jun 2, 1984 | 4835/4885 | 50 | 8.5 | 15.9 \times 4.4, 44 | 0.07 |

Fig. 1b zooms on the central double source (S3). The region corresponds to the magenta box in Fig. 1a. The contours and gray-scale image are the emission detected at 610 MHz at full resolution ($8'' \times 4''$). Thanks to the higher sensitivity, more extended emission associated with the double is visible in this new 610 MHz image, compared to the previous observations published in G11 (also reported in Fig. 9).

The $2''$ -resolution image from the *VLA*-A data at 1.5 GHz (Fig. 1c, contours) shows the innermost structure of the source. The contours are overlaid on the *VLA*-BnC image at 4.9 GHz at resolution $5'' \times 2''$. At ~ 1 kpc scale, the source appears a core-jet with position angle of $\sim 30^\circ$, which is approximately aligned with the axis of the double on larger scale (panel b). A faint blob of emission is visible to the east at 1.5 GHz, apparently detached from the core-jet. The blob is not detected at 4.9 GHz.

3.2. The large-scale emission

The *GMRT* 330 MHz image, produced at the lower resolution of $45'' \times 45''$, is presented in Fig. 2. The new images at 240 MHz and 610 MHz are shown at similar resolution in Fig. 3 and Fig. 4a. The large-scale emission is detected at high levels of significance at all frequencies. Its total extent is ~ 80 kpc, consistent in all images. The brightest regions of this component are also visible in the *VLA*-CnD image at 1.4 GHz, restored with a circular beam of $60''$ (Fig. 4b). It is clear that the large-scale emission becomes progressively fainter with increasing frequency. The morphology also seems to change from the 1.4 GHz image, where the source shows a bipolar structure with east-west axis, to the 240 MHz image, where the extended emission becomes fairly amorphous and more extended in the north-south direction. This suggests that the radio spectrum of this component is very steep.

4. RADIO SPECTRAL PROPERTIES, MAGNETIC FIELDS AND RADIATIVE AGE

We studied the spectral properties – total integrated spectrum and spectral index distribution – and derived the physical parameters of NGC 1407 using the Synage++ package (Murgia 2001).

1. We fitted the radio spectrum of the inner double and large-scale emission separately, and derived the injection spectral index α_{inj} and break frequency ν_{break} for each component.
2. We obtained a spectral index image of the system and extracted the distribution of α along the source structure as a function of the distance from the center. By fitting the observed spectral index trend, we derived ν_{break} for the large-scale emission.
3. We calculated the magnetic field B_{eq} assuming that the relativistic particle and magnetic field energy densities are in approximate energy equipartition. We assumed cylindrical geometry, a filling factor of unity and that there is equal energy in relativistic ions and electrons ($k = 1$). We also assumed that the magnetic field is un-ordered along the line of sight. We used the radio luminosity at 240 MHz, α_{inj} from the spectral modelling, and imposed a low-energy cutoff of $\gamma_{\text{min}}=100$ in the energy distribution of the radiative electrons, where γ is the electron Lorentz factor (e.g., Brunetti et al. 1997; Beck & Krause 2005). This allows us to take into account the contribution from relativistic electrons with an energy as low as ~ 50 MeV.
4. Under a number of assumptions, the knowledge of the break frequency in the spectrum of a radio source allows us to estimate the time elapsed since the source formation (e.g., Myers & Spangler 1985). We assumed that radiative (i.e., synchrotron and inverse Compton) losses dominate over expansion losses, and that the

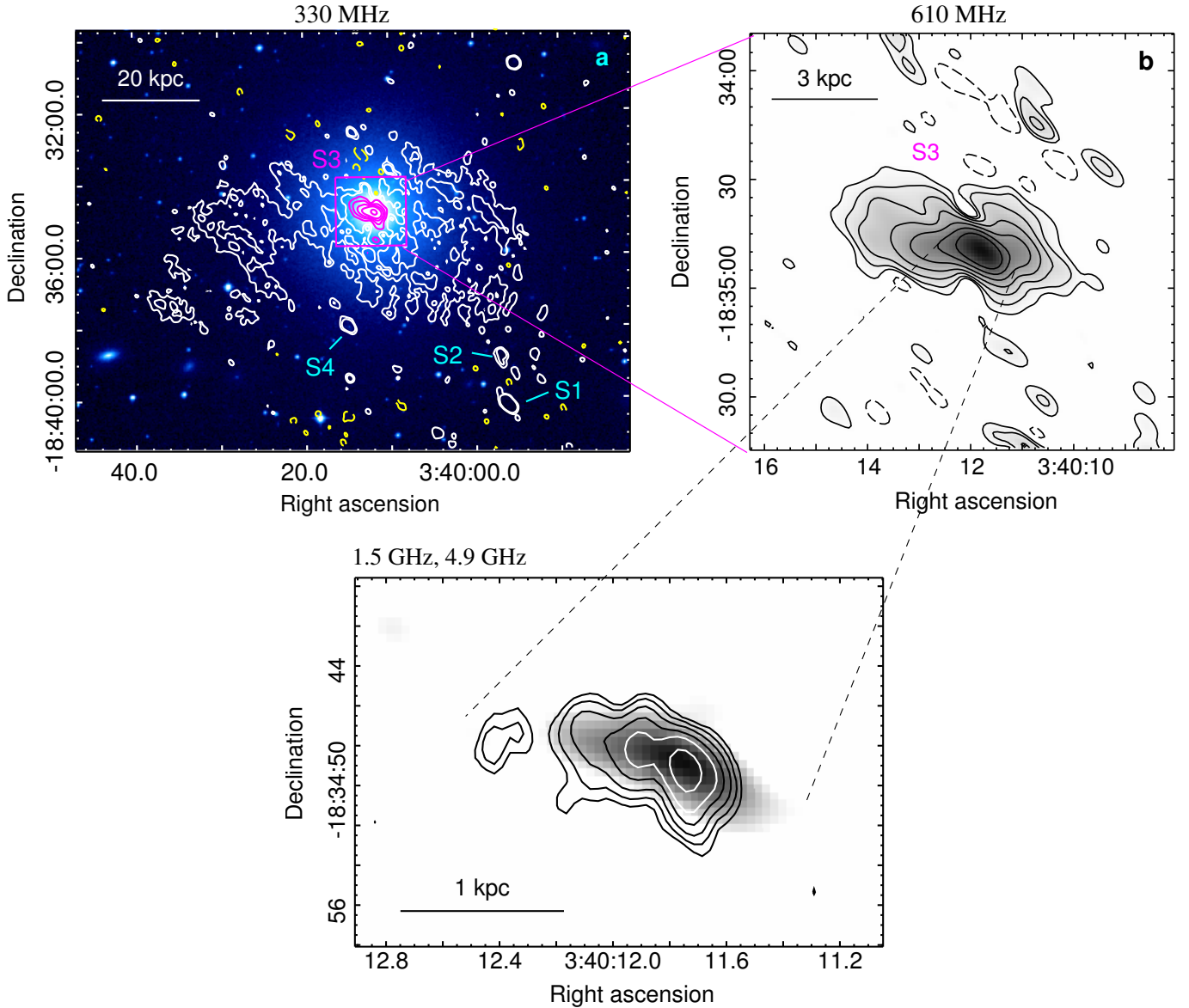


FIG. 1.— *a*: GMRT 330 MHz full resolution contours (white, magenta and yellow), overlaid on the optical POSS-2 image. The restoring beam is $12.1'' \times 9.2''$, p.a. 42° . The rms noise level is $0.2 \text{ mJy beam}^{-1}$. Contour levels are -0.6 (dashed yellow), 0.6 , 1.2 , 2.4 (white), 4.8 , 9.6 , 20 and 80 (magenta) mJy beam^{-1} . Labels indicate the discrete radio sources embedded in the extended structure. *b*: GMRT 610 MHz full resolution image (contours and gray scale) of the inner double (S3). The restoring beam is $8.2'' \times 4.4''$, p.a. 46° . The rms noise level is $0.05 \text{ mJy beam}^{-1}$. Contour levels are spaced by a factor of 2 starting from $0.2 \text{ mJy beam}^{-1}$. Dashed contours correspond to $-0.2 \text{ mJy beam}^{-1}$. *c*: VLA 1.5 GHz contours (FWHM = $2.2'' \times 1.3''$, $1\sigma = 0.1 \text{ mJy beam}^{-1}$) overlaid on the VLA gray-scale image at 4.9 GHz (FWHM = $5.1'' \times 2.0''$, $1\sigma = 0.14 \text{ mJy beam}^{-1}$). Contours scale by a factor of 2 starting from $0.3 \text{ mJy beam}^{-1}$.

magnetic field strength is uniform across the source and remains constant over the source life time. We also assume that the relativistic electron population is isotropic (Jaffe & Perola 1973) and reacceleration processes can be neglected. We used the following equation

$$t_{\text{rad}} = 1590 \frac{B_{\text{eq}}^{0.5}}{(B_{\text{eq}}^2 + B_{\text{CMB}}^2)} [(1+z)\nu_{\text{break}}]^{-0.5}$$

to derive the radiative age t_{rad} of both radio components, where t_{rad} is expressed in Myr, ν_{break} in GHz, and B_{eq} and B_{CMB} in μG . $B_{\text{CMB}} = 3.2(1+z)^2$ is the equivalent magnetic field of the cosmic microwave background

(CMB) radiation, i.e., the magnetic field strength with energy density equal to that of the CMB at the redshift z .

Our analysis is presented in detail in the following subsections, and results are summarized in Table 5, which provides the radio luminosity at 240 MHz, volume, observed spectral index, radiative model used for the spectral fitting, injection spectral index, break frequency, equipartition magnetic field, radiative age and equipartition pressure for each component.

4.1. Integrated spectra

We measured the flux density of the inner double and large-scale emission in similar regions at all frequencies, i.e., the extent of the double at 610 MHz (Fig. 1b) and area covered

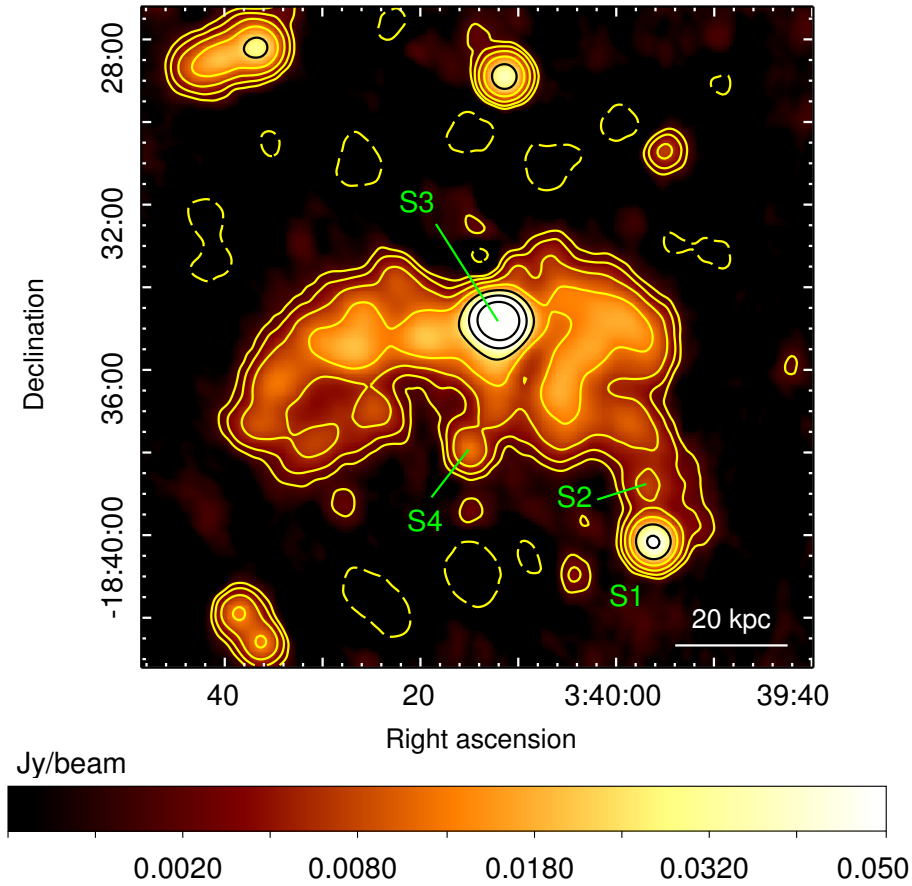


FIG. 2.— *GMRT* low-resolution image at 330 MHz. The image has been restored with a beam of $45.0'' \times 45.0''$, p.a. 0° . The rms noise level is $0.5 \text{ mJy beam}^{-1}$. Contours start at $+3\sigma$ and then scale by a factor of 2. The -3σ level is shown by the dashed contours. Labels indicate the discrete radio sources (Fig. 1a).

by the diffuse emission at 240 MHz (Fig. 3). The flux densities are summarized in Table 4, along with the associated uncertainties (1σ) and angular resolution of the images used for the measurements.

The *VLA* image at 327 MHz (not shown here) detects the inner double, but does not show significant diffuse emission around it, due to its lower sensitivity compared to the *GMRT* 330 MHz image (Tab. 3). For this reason, Table 4 provides only the flux density at 327 MHz for the central double.

We also inspected the VLSS⁹ image at 74 MHz and found a weak source at the position of the inner double, with a peak flux density of $\sim 400 \text{ mJy beam}^{-1}$. The source is not listed in the VLSS catalog, implying that its total flux density at 74 MHz is less than the 5σ local rms level ($1\sigma=86 \text{ mJy beam}^{-1}$). We therefore assume an upper limit of $S_{74\text{MHz}}=430 \text{ mJy}$ for the double. No evidence of significant emission over the large-scale structure is visible on the VLSS image. Given that the total area occupied by the diffuse component corresponds to ~ 24 VLSS beams (each beam is $80'' \times 80''$), we can place a 3σ upper limit of 6 Jy at 74 MHz.

In Fig. 5 we show the integrated radio spectra of the inner double (red points) and large-scale emission (black points).

The data points at 1.5 GHz and 4.9 GHz from A and BnC configurations (Tables 2 and 4) are not shown in the plot; due to the high angular resolution and lack of short spacings, the images from these datasets detect only the innermost region of the double (Fig. 1c).

The overall spectrum of the inner double has $\alpha_{\text{obs}} = 0.69 \pm 0.03$ between 240 MHz and 4.9 GHz. A spectral steepening seems to occur at high frequency, with α_{obs} changing from 0.65 ± 0.05 below 1425 MHz to 0.75 ± 0.06 above. The large-scale emission has a much steeper spectrum, with $\alpha_{\text{obs}} = 1.80 \pm 0.05$ in the 240 MHz-1.4 GHz range. The upper limit at 74 MHz suggests a low-frequency flattening of the spectrum, with $\alpha_{\text{obs}} \lesssim 1.6$ below 240 MHz.

4.1.1. Spectral modelling

We fitted the spectrum of the inner double using a continuous injection (CI) model (e.g., Kardashev 1962), in which the source is continuously replenished by a constant flow of fresh relativistic electrons with a power-law energy distribution in a region of constant magnetic field. Under these assumptions, the radio spectrum has a standard shape, with a low-frequency spectral index representing the α_{inj} of the youngest electron population, and a high-frequency spectral index limited to be $\leq \alpha_{\text{inj}} + 0.5$ at frequencies above ν_{break} .

The resulting best-fit for the inner double (red line in Fig. 5)

⁹ *VLA* Low-frequency Sky Survey (Cohen et al. 2007)

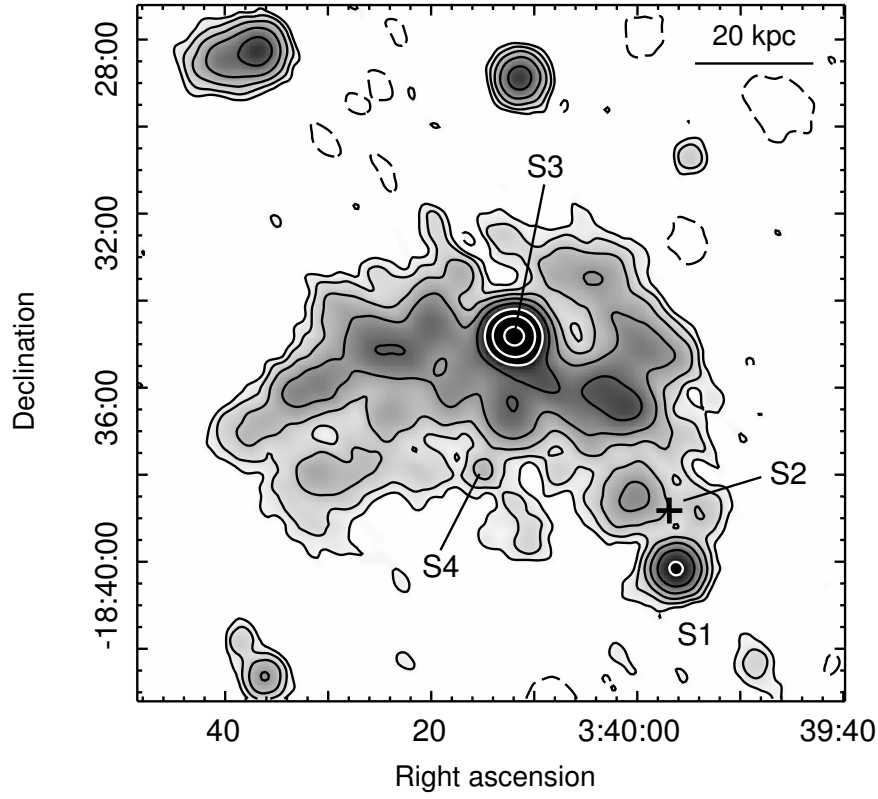


FIG. 3.— *GMRT* low-resolution image (contours and gray scale) at 240 MHz. The restoring beam is $45.0'' \times 45.0''$, p.a. 0° . The rms noise level is 1 mJy beam^{-1} . Contours start at $+3\sigma$ and then scale by a factor of 2. The -3σ level is shown by the dashed contours. Labels indicate the discrete radio sources (Fig. 1a).

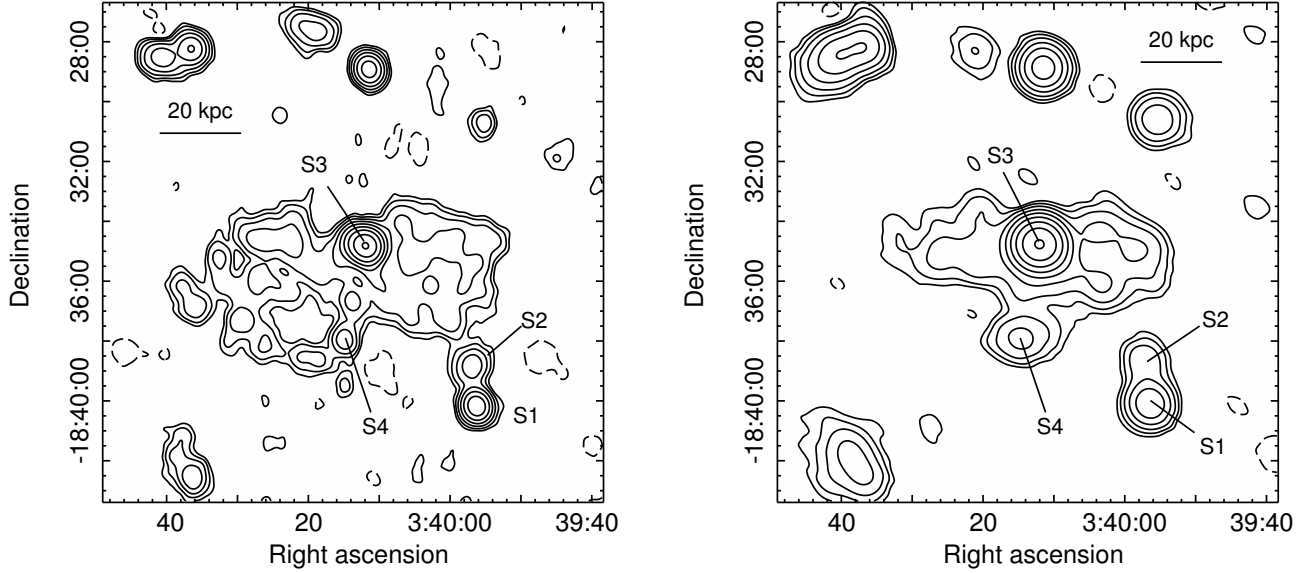


FIG. 4.— *a*: *GMRT* low resolution contours at 610 MHz. The restoring beam is $41.8'' \times 37.0''$, p.a. 17° . The rms noise level is $0.15 \text{ mJy beam}^{-1}$. *b*: *VLA-CnD* low resolution contours at 1425 MHz. The image has been restored with a circular beam of $60''$. The rms noise level is $0.08 \text{ mJy beam}^{-1}$. In both panels contours start at $+3\sigma$ and then scale by a factor of 2. The -3σ level is shown as dashed contours. Labels indicate the discrete radio sources (Fig. 1a).

yields a non-aged spectral index $\alpha_{\text{inj}} = 0.55^{+0.14}_{-0.05}$ and $\nu_{\text{break}} \sim 5.6 \text{ GHz}$. With these values, the estimated equipartition mag-

netic field and radiative age of the central double are $B_{\text{eq}} \sim 7 \mu\text{G}$ and $t_{\text{rad}} \sim 30 \text{ Myr}$ (Table 5).

TABLE 4
FLUX DENSITIES OF THE NGC 1407 SYSTEM

| component | ν (MHz) | S_ν (mJy) | FWHM (" × ") |
|-----------------------|----------------|------------------|--------------------------------------|
| inner double (S3) . . | 74 | < 430 | 80 × 80 (VLSS) |
| | 240 | 270 ± 22 | 15.4 × 12.5 (<i>GMRT</i> this work) |
| | 327 | 207 ± 12 | 28 × 17 (<i>VLA</i> this work) |
| | 330 | 230 ± 18 | 12.0 × 9.2 (Fig. 1a) |
| | 610 | 153 ± 8 | 8.2 × 4.4 (Fig. 1b) |
| | 1400 | 87 ± 4 | 45 × 45 (NVSS) |
| | 1425 | 85 ± 4 | 60 × 60 (Fig. 4b) |
| | 1.50 | 37 ± 2 | 2.2 × 1.3 (Fig. 1c) |
| large-scale emission | 4860 | 34 ± 2 | 15.9 × 4.4 (<i>VLA</i> this work) |
| | 4860 | 23 ± 1 | 5.1 × 2.0 (Fig. 1c) |
| large-scale emission | 74 | < 6000 | 80 × 80 (VLSS) |
| | 240 | 945 ± 76 | 45.0 × 45.0 (Fig. 3) |
| | 330 | 668 ± 53 | 45.0 × 45.0 (Fig. 2) |
| | 610 | 194 ± 10 | 41.8 × 37.0 (Fig. 4a) |
| | 1425 | 38 ± 2 | 60.0 × 60.0 (Fig. 4b) |

Notes – The flux density of the large-scale emission has been obtained after subtraction of the contribution of the inner double (S3) and point sources S1, S2 and S4.

The very steep spectral index of the large-scale component ($\alpha_{\text{obs}} = 1.8$) suggests that this emission is old. For this reason, we modelled its spectrum using a CI_{OFF} model (e.g., Parma et al. 2007; Murgia et al. 2011). This model assumes an initial phase of electron injection at a constant rate by the nuclear source (CI phase), followed by a switch-off of the nuclear activity. A dying phase then begins, with the radio emission rapidly fading subject to the energy losses of the relativistic electrons. It is assumed that the magnetic field strength is uniform within the source, energy losses are dominant with respect to other processes, and the pitch angle of the radiating electrons has an isotropic distribution with respect to the local direction of the magnetic field. We imposed an initial spectral index $\alpha_{\text{inj}} = 0.7$, similar to the observed α of the inner double (Tab. 5), and derived an upper limit of 230 MHz for the break frequency. The estimated magnetic field is $B_{\text{eq}} \sim 2.1 \mu\text{G}$ and the total radiative lifetime is very long, i.e., $t_{\text{rad}} > 320 \text{ Myr}$.

The CI_{OFF} model also provides $t_{\text{OFF}}/t_{\text{rad}}$, i.e., the dying to total source age ratio (for details see Parma et al. 2007). We found that the active phase lasted for at least 128 Myr and the nuclear activity switched off not more than $t_{\text{off}} \sim 192 \text{ Myr}$ ago.

4.2. Spectral index image

We obtained images of the radio spectral index distribution by comparing sets of *GMRT* images at different frequencies, produced with the same cell size, uv range, restoring beam, and corrected for the primary beam attenuation. The images were aligned, the pixels with brightness below the 5σ level were blanked, and finally the images were combined into a spectral index image. In Fig. 6a we present our best spectral index image obtained by comparing the images at 330 MHz and 610 MHz, both restored with a circular beam of $45''$ radius and with noise levels similar to the images in Fig. 2 and Fig. 4a. We also show the distribution of the spectral index uncertainty based on the rms noise in both radio images (Fig. 6b) and overlay the 330 MHz contours on both images to provide

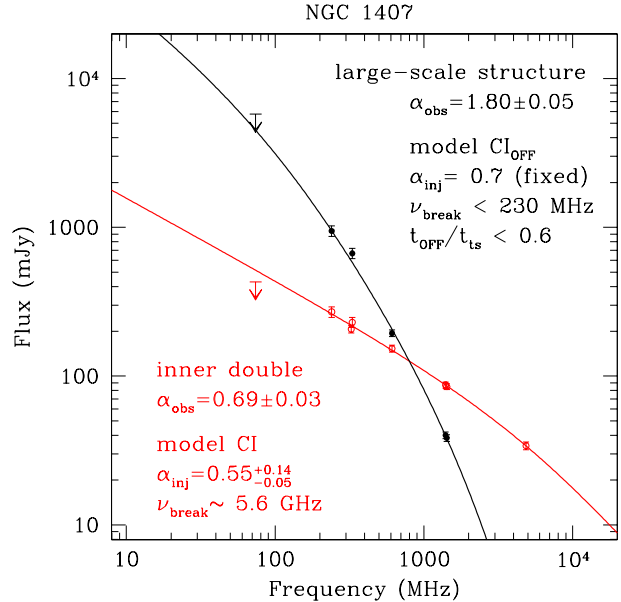


FIG. 5.— Integrated spectra of the inner double (red circles) and diffuse component (black circles) using the flux density reported in Table 4. The solid lines are the best-fit CI (red) and CI_{OFF} (black) models described in the text (Sect. 4.1.1).

a reference for the source morphology. We note that Fig. 6b does not include the absolute flux scale uncertainty of 5% at 610 MHz and 8% at 330 MHz, which results in a typical error on the spectral index of $\sigma_\alpha = 0.15$.

The inner double (S3), unresolved at this resolution, has an average spectral index of $\sim 0.75 \pm 0.02$, consistent with $\alpha_{\text{obs}} = 0.66 \pm 0.15$ given by the flux densities measured at the two frequencies (Table 4). Sources S1 and S4 have both $\alpha \sim 0.8$, while the weak source S2 has $\alpha \sim 0.6$. The large-scale component has spectral index values ranging between $\alpha \sim 1.5$ and $\alpha \sim 2.5$, with uncertainties of $\sim 0.06 - 0.08$ in the brightest regions and up to ~ 0.25 at the edges.

Fig. 7 shows the spectral index profiles along the eastern and western portions of the diffuse emission. We first measured the flux density in circular regions on the individual images at 240 MHz and 610 MHz (see inset), both restored with a circular beam of $45''$ -radius, and then computed the corresponding spectral index. The circles were placed following the brightest regions along the diffuse emission. The radius of each circle was set to $55''$ to ensure a sufficient signal-to-noise ratio and independent data points. In the plot we also show the data point corresponding to the inner double S3, obtained from the same images. As noticed in Section 4.1, there is a clear and abrupt separation in α between S3 and outer emission, the latter being substantially steeper, with $\alpha = 1.5 \pm 0.1$ to 2.2 ± 0.1 along the western region and $\alpha = 1.8 \pm 0.1$ to 2.2 ± 0.1 in the eastern one.

We interpreted the spectral index trend in Fig. 7 in terms of radiative aging of the relativistic electrons by synchrotron and inverse Compton processes (e.g., Parma et al. 2007, and references therein), assuming that radiative losses dominate over expansion losses and reacceleration. If the magnetic field and expansion velocity of the relativistic plasma are both constant, we can then estimate the minimum break frequency from the fit of the observed spectral index profiles. We used the re-

TABLE 5
SPECTRAL MODELLING RESULTS, EQUIPARTITION MAGNETIC FIELDS AND RADIATIVE AGES

| | $L_{240\text{MHz}}$ (W Hz^{-1}) | V (kpc^3) | α_{obs} | spectral model | α_{inj} | ν_{break} (GHz) | B_{eq} (μG) | t_{rad} (Myr) | $t_{\text{OFF}}/t_{\text{rad}}$ | t_{CI} (Myr) | t_{OFF} (Myr) | P_{radio} (erg cm^{-3}) |
|-------------------------|---|---------------------------|-----------------------|--|------------------------|-------------------------------|--------------------------------------|---------------------------|---------------------------------|--------------------------|---------------------------|--|
| inner double | 2.02×10^{22} | 140 | 0.69 ± 0.03 | CI | $0.55^{+0.14}_{-0.05}$ | 5.6 | 7 | 30 | – | – | – | 2.8×10^{-12} |
| large-scale emission | 7.07×10^{22} | 84×10^3 | 1.80 ± 0.05 | CI_{OFF}^a CI_{OFF}^b | 0.7^c 0.7^c | < 0.23 0.34 | 2.1 | > 320 264 | < 0.60 0.65 | > 128 92 | < 192 172 | 2.5×10^{-13} |

Notes to Table 5– *a*: fit of the total integrated spectrum; *b*: fit of the spectral index trend; *c*: fixed.

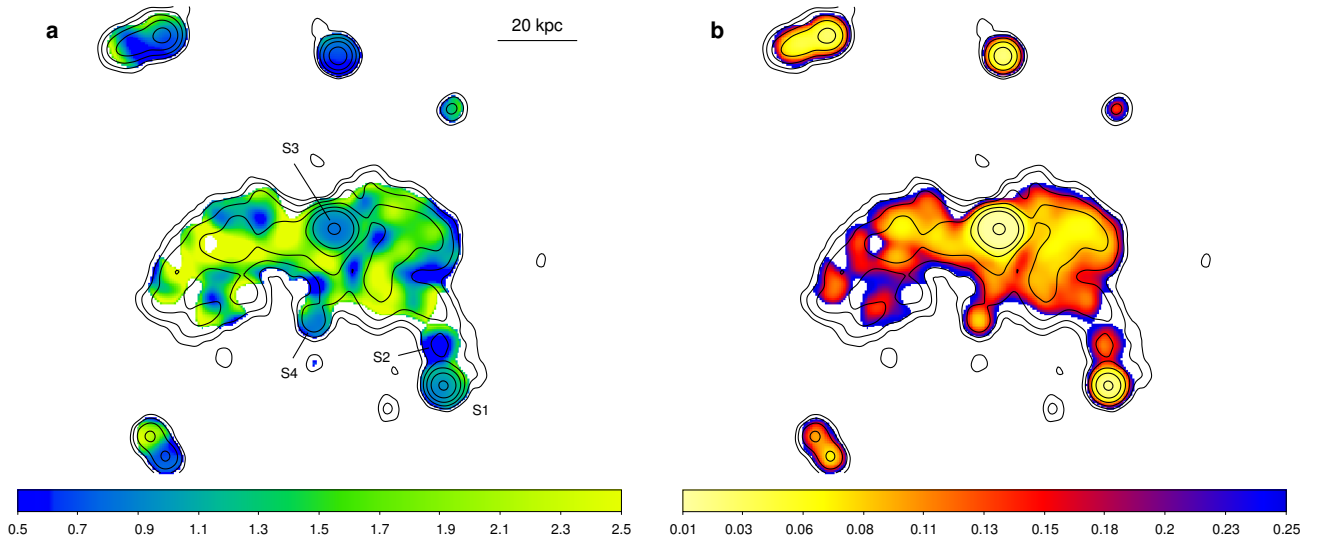


FIG. 6.— Color scale image of the spectral index (a) and spectral index uncertainty (b) distributions between 330 MHz and 610 MHz. The image has been computed from images with a restoring beam of $45'' \times 45''$. Contours at 330 MHz and labels are as in Fig. 2. The spectral index uncertainty map is based on the rms noise in both radio images. The absolute flux calibration uncertainty is not included.

lation $\nu_{\text{break}} \propto d^{-2}$, where d is the distance from the core, which reflects the fact that the radiating electrons age as they travel away from the nucleus. The two profiles along the large-scale component were fitted separately adopting a CI_{OFF} model (Sect. 4.1.1) with α_{inj} fixed to 0.7, i.e., the spectral index of S3. The best fit, shown as blue lines in Fig. 7, gives a similar break frequency in the east and west portions of the source – $\nu_{\text{break}} = 330 \pm 30$ MHz and $\nu_{\text{break}} = 340 \pm 30$ MHz, respectively – and a ratio $t_{\text{off}}/t_{\text{rad}}$ of 0.6 and 0.5. Using the average between these values and a magnetic field strength of $2.1 \mu\text{G}$ (Table 5), we estimated a total age of ~ 264 Myr. The CI phase lasted approximately 92 Myr and the nuclear engine switched off ~ 172 Myr ago.

The total age derived here is shorter than the lower limit of ~ 320 Myr obtained from the fit of the total spectrum (Table 5). A reason for such discrepancy may lie in the use of different areas to extract the flux densities in the two cases; the region used to derive the total spectrum corresponds to the whole area occupied by the diffuse emission at 240 MHz, including the emission which is the most distant from the center and, thus, plausibly the oldest. The circular regions in Fig. 7 sample instead only a part of that region.

Another consideration is that the spectral index between 240 MHz and 610 MHz ($\alpha_{\text{obs}} = 1.70 \pm 0.10$) is slightly flat-

ter than the average slope of the total spectrum, i.e., $\alpha_{\text{obs}} = 1.80 \pm 0.05$ between 240 MHz and 1.4 GHz. This could result in a break frequency from the spectral trend fitting which is higher than that estimated from the total spectrum, thus yielding a shorter age (for the same magnetic field strength).

Finally, it is important to bear in mind that both methods rely on the age determination from the break frequency, which has large uncertainties due to the number of underlying assumptions (see discussion in Section 7.1).

5. X-RAY OBSERVATIONS AND DATA ANALYSIS

NGC 1407 was observed during *Chandra* cycle 1, on 2000 August 16, for ~ 49 ks (ObsID 791), with the ACIS-S instrument operating in very faint telemetry mode. A summary of the *Chandra* mission and instrumentation can be found in Weisskopf et al. (2002). The data were reduced and analysed using CIAO 4.2 and CALDB 4.3 following techniques similar to those described in O’Sullivan et al. (2007) and the *Chandra* analysis threads¹⁰. The first half of the observation suffered from significant background flaring, and the final cleaned exposure time was 30.9 ks.

Point sources were identified using the WAVDETECT task, with a detection threshold of 1×10^{-6} , chosen to ensure that

¹⁰ <http://asc.harvard.edu/ciao/threads/index.html>

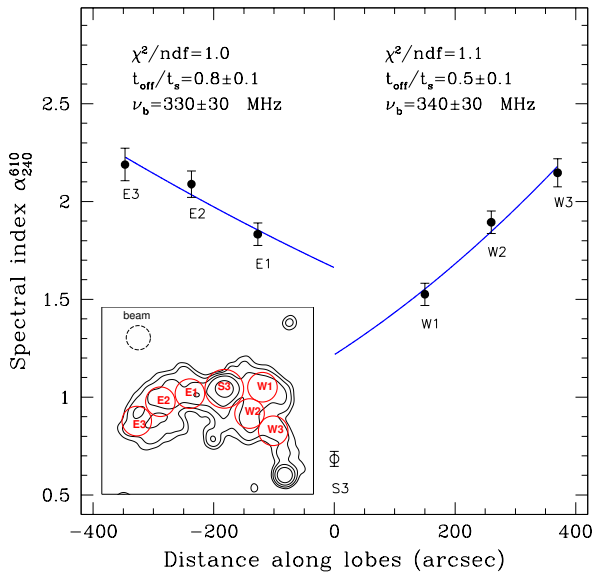


FIG. 7.— 240 MHz-610 MHz spectral index distribution as function of the distance from the center, computed using the $55''$ -radius circular boxes shown in the inset. The solid line is the best fit of the radiative model described in the text.

the task detects ≤ 1 false source in the ACIS-S field, working from a 0.3-7.0 keV image and exposure map. All point sources were excluded except the source corresponding to the AGN. Spectra were extracted using the SPEXTRACT task. Spectral fitting was performed in XSPEC 12.7.0e. Abundances were measured relative to the abundance ratios of Grevesse & Sauval (1998). A galactic hydrogen column of $0.0542 \times 10^{22} \text{ cm}^{-2}$ and a redshift of 0.0059 were assumed in all fits. Spectra were grouped to 20 counts per bin, and counts at energies outside the range 0.5-7.0 keV were ignored during fitting.

Background spectra were drawn from the standard set of CTI-corrected ACIS blank sky background events files in the *Chandra* CALDB. The exposure time of each background events file was altered to produce the same 9.5-12.0 keV count rate as that in the target observation. Very faint mode background screening was applied to both source and background data sets.

XMM has also observed NGC 1407 (ObsId 0404750101), with an exposure of ~ 66 ks. A detailed summary of the *XMM* mission and instrumentation can be found in Jansen et al. (2001, and references therein). The observation is centred close to NGC 1400, with NGC 1407 $\sim 9'$ off-axis. To provide a comparison with *Chandra* image analysis, we reduced this data using SAS v10 following the methods described in O'Sullivan et al. (2011). The EPIC-MOS instruments were operated in full frame and the EPIC-pn in extended full frame mode, with the thin optical blocking filter. Periods including background flaring, when the total count rate deviated from the mean by more than 3σ , were excluded, leaving useful exposures of ~ 38 ks (MOS) and ~ 26 ks (pn). Point sources were identified using EDETECT_CHAIN, and regions corresponding to the 85 per cent encircled energy radius of each source (except that at the peak of the diffuse emission) were excluded.

6. X-RAY ANALYSIS

6.1. The X-ray images

We initially examined the structure of the hot intra-group medium (IGM) using exposure-corrected 0.3-2 keV *Chandra* and *XMM-Newton* images. Previous *ROSAT* observations have shown NGC 1407 to be more X-ray luminous than NGC 1400, and that there is a clump of emission between the two (e.g., Mulchaey et al. 2003). Figure 8 shows the *XMM* image, adaptively smoothed using the SAS ASMOOTH task with a signal-to-noise ratio of 10. The image confirms the features observed in the *ROSAT* data. The 240 MHz emission (contours) extends well beyond the brightest part of the X-ray emission associated with NGC 1407.

The clump of emission between NGC 1407 and NGC 1400 consists of both point sources and diffuse emission. Although brighter to the east of NGC 1400, the diffuse emission extends across the galaxy and to the west as far as the edge of the field of view. The origin of this trail is unclear. NGC 1400 is known to have a velocity offset from the group mean by $\sim 1100 \text{ km s}^{-1}$ (Quintana et al. 1994), which is ~ 3 times the velocity dispersion of the group ($\sigma_v \sim 370 \text{ km s}^{-1}$) and ~ 2 times the sound speed v_{sonic} (for a 1.2 keV gas, $v_{\text{sonic}} \sim 520 \text{ km s}^{-1}$). Therefore, the trail could be tidally or ram-pressure stripped material. However, there is no clear connection with NGC 1407.

Figure 9a shows the *Chandra* image, smoothed with a $10''$ Gaussian. The emission is asymmetric, being swept back from the northern side, forming two wings to the east and west, and more extended to the south. There is some indication of an edge, or drop in surface brightness, on the northern side. To investigate this structure further, we modelled and subtracted the mean surface brightness distribution to reveal any residual structures. Two β -models were used to represent the galaxy and group emission, and a flat model for the background. Fitting was carried out in CIAO SHERPA, correcting for exposure using a monoenergetic 0.85 keV exposure map (the energy was chosen to match the peak photon energy of the data). After subtraction of the model, the residual map is smoothed to bring out any remaining structures. The result is shown in Figure 9b. An arc of positive residuals extends across the northern side of the galaxy, with strong negative residuals to its north and south. The arc is narrow in the centre, and broader in the wings, particularly on the east side. This again suggests the presence of a surface brightness edge on the north side of the galaxy, with denser or cooler gas forming the bright arc, and the northern negative residual indicating the sharp drop seen in Figure 9a. The negative residual in the galaxy core is likely caused by the bright arc and central point sources biasing the inner part of the model to high values. We note that using an elliptical beta model does not result in any significant changes to the structures but fails to model the core and central point source properly.

Figure 10 shows the 0.3-2 keV exposure-corrected surface brightness profile extracted across the northern arc, using a 125° sector, with the mean surface brightness profile across the remainder of the galaxy for comparison. The surface brightness drops further in the north than in the rest of the halo, and the profile first steepens (between ~ 5 -10 kpc), then flattens outside ~ 10 kpc. There is no clear discontinuity in the profile, which would indicate the presence of a shock or cold front. However, the exposure may simply be too shallow to detect such a feature; relatively wide spatial bins are required to determine reliable surface brightness values.

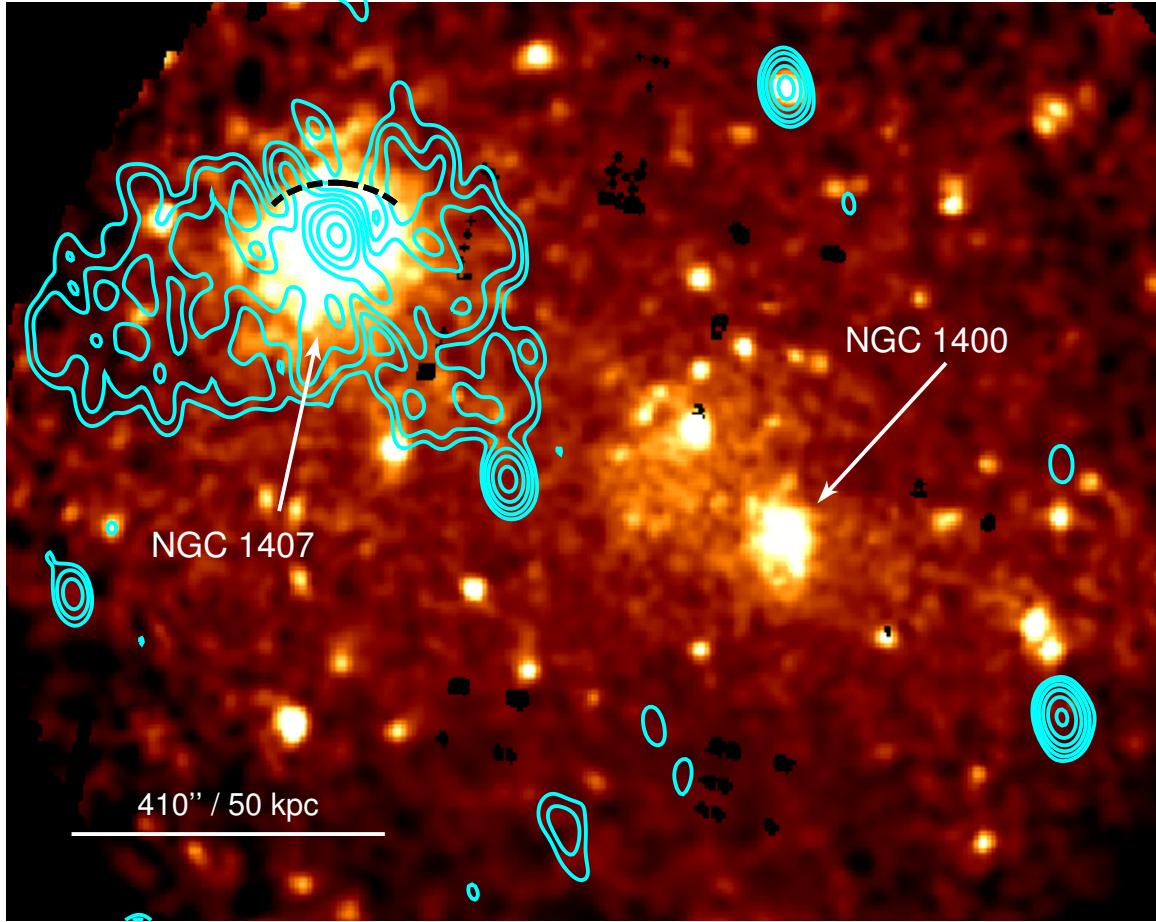


FIG. 8.— *XMM-Newton* adaptively smoothed 0.3–2 keV image of the NGC 1407 group, with *GMRT* 240 MHz contours overlaid from G11 (FWHM= $48.5'' \times 31.9''$). Contours start at $3\sigma = 3 \text{ mJy beam}^{-1}$, and then scale by a factor of 2. NGC 1400, a group member, is marked, as well as the trail of X-ray emission associated with it. The black dashed arc marks the surface brightness edge in Fig. 9.

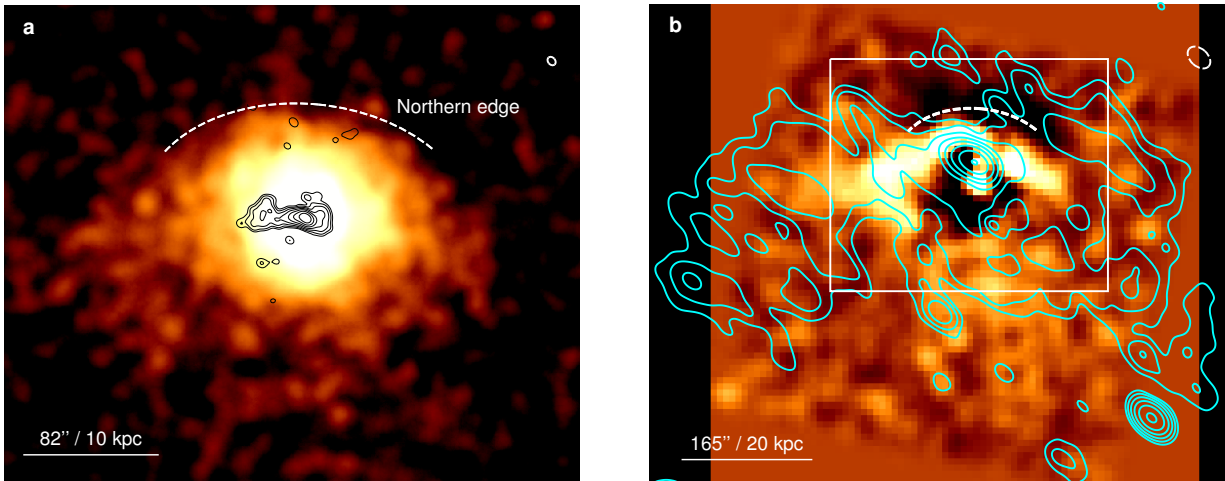


FIG. 9.— *a*: 0.3–2 keV *Chandra* image of NGC 1407, Gaussian-smoothed with a $10''$ kernel, with overlaid the 610 MHz contours at the resolution of $5.6'' \times 4.3''$ from G11. Contours are spaced by a factor of 2 starting from $3\sigma=0.3 \text{ mJy beam}^{-1}$. The white arc marks the approximate position of the surface brightness edge, $\sim 70''$ north of the galaxy core. *b*: 0.3–2.0 keV *Chandra* surface brightness residuals after fitting and subtracting two circular β -models and a flat model for the background, binned by a factor 16 and smoothed with a Gaussian with a radius of 3 pixel ($23.66''$). Contours at 330 MHz, at the resolution of $33'' \times 22''$, are overlaid starting at $1.5 \text{ mJy beam}^{-1}$ and then scaling by a factor of 2. The white box indicates the area of panel *a*. In both panels the radio beam is indicated by the white dashed ellipse.

6.2. Gas properties

To determine the physical properties of the IGM, we extracted a radial spectral profile centred on the galaxy. Since both the gas around NGC 1407 and the larger-scale group

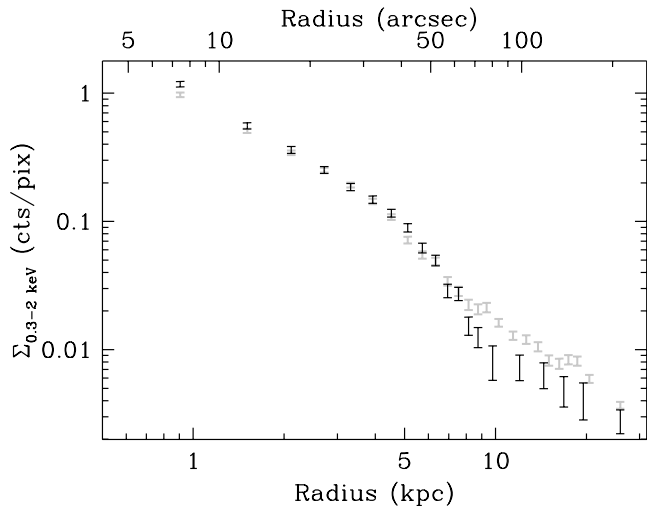


FIG. 10.— Exposure-corrected 0.3-2 keV surface brightness in a 125° arc northward (black) and averaged over the remainder of the galaxy (grey). Error bars indicate 1 σ uncertainty.

emission show signs of disturbed, asymmetric structures, we chose to use simple circular annuli containing 1000-3000 net counts. The radio emission is observed throughout the core and over much of the *Chandra* field of view, therefore we do not exclude the corresponding region, since to do so would restrict the profile to the outer parts of the group. However, we note that if cavities are present coincident with the radio emission, this will affect the results of the spectral fits, both in terms of density (owing to the partial filling factor of the X-ray emitting plasma) and temperature (since the distribution of temperatures along the line of sight will change). The spectra were fitted with a deprojected, absorbed APEC model. Abundances were tied between bins where necessary to stabilise the deprojection. The typical abundance was $\sim 0.6 Z_{\odot}$. Figure 11 shows the resulting temperature and density profiles, and the pressure profile derived from them. Pressure was calculated as $P = nkT$ where $n = 2n_e$.

The temperature profile is in reasonable agreement with previous spectral studies (e.g., Rasmussen & Ponman 2007; Diehl & Statler 2008), showing a cool core surrounded by hotter intra-group emission. Both density and pressure profiles follow unexceptional approximate powerlaws.

6.3. X-ray temperature map

To examine the spatial variation of temperature in the gas, we prepared a temperature map using the technique developed by David et al. (2009) which takes advantage of the close correlation between the strength of lines in the Fe-L complex and gas temperature in ~ 1 keV plasma. Most of the emission from such gas arises from the L-shell lines from Fe-XIX (Ne-like) to Fe-XXIV (He-like). For CCD resolution spectra, these lines are blended to form a single broad peak between approximately 0.7 and 1.2 keV. The centroid or mean photon energy of this peak increases with the temperature of the gas as the dominant ionisation state of Fe shifts from Fe XIX in 0.5 keV gas to Fe XXIV in 1.2 keV gas, with Fe XVII and Fe XVIII providing the strongest line emission at the temperatures seen in the core of NGC 1407. The mean photon energy of the blended L-shell lines is independent of energy above ~ 1.3 keV.

We can thus estimate the temperature distribution of the gas by mapping the mean photon energy in the 0.7-1.2 keV band.

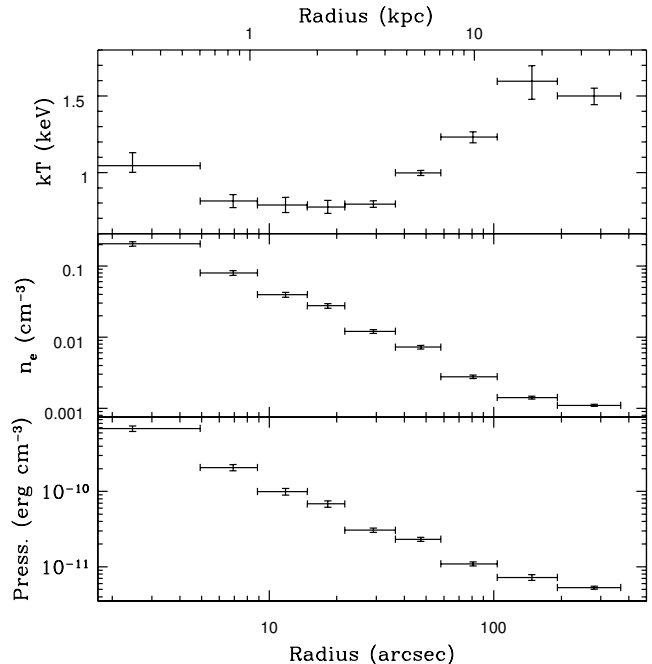


FIG. 11.— Radial profiles of temperature, density and pressure in NGC 1407. Density and pressure in the outermost bin may be overestimated since it includes emission from the outer parts of the IGM along the line of sight.

We estimated the mean gas properties from the spectral fits described in Section 6.2, taking an abundance $0.6 Z_{\odot}$ as representative and simulated spectra for a range of temperatures, with redshift set to that of NGC 1407 and the hydrogen column set to the Galactic value. These showed that for temperatures between ~ 0.5 and ~ 1.3 keV, the relationship is approximately linear ($kT = -6.38 + 7.83 < E >$). Prior testing in other systems suggests that the relationship is relatively insensitive to variations in abundance and hydrogen column (O’Sullivan et al. 2009).

Using this technique, we produced the map shown in Figure 12. The temperature in the galaxy core is 0.5-0.7 keV, rising to 1.2-1.3 keV north and south of the galaxy. We note that the highest temperatures in the map are somewhat lower than those in the radial profile (Fig. 11), since the mapping technique becomes insensitive to temperature increases above ~ 1.3 keV. The cool core region is relatively circular. The black dashed arc marks the location of the X-ray surface brightness edge. The gas behind the edge seems to be cooler (~ 0.9 -1 keV) than the gas right in front (~ 1.2 keV), suggesting that the feature may be a cold front. However, the exposure is too shallow to allow temperature measurements on a scale comparable to the size of the feature. We therefore cannot rule out the alternative possibilities that there is no strong discontinuity, or that a weak shock is present. A deeper *Chandra* pointing would be required to constrain the gas temperature behavior across the edge and determine the real nature of this feature.

The cool (~ 1 keV) regions immediately east and west of the galaxy core correspond with the wings of the arc of excess surface brightness seen in Figure 9, showing that it is caused at least in part by the increased emissivity of this cooler material. This may indicate that material has been drawn out of the galaxy core and either heated or mixed with warmer IGM gas.

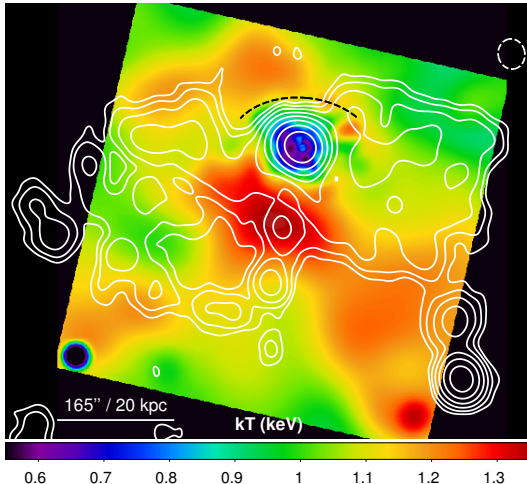


FIG. 12.— *Chandra* adaptively smoothed Fe-peak temperature map, with the low resolution 610 MHz contours overlaid (same as Fig. 4a). The black dashed arc marks the surface brightness edge in Fig. 9. The radio beam is indicated by the white dashed ellipse.

7. DISCUSSION

7.1. Restarted activity in NGC 1407

The radio images presented in Section 3 show faint, diffuse emission, approximately 80 kpc across, which wholly encloses and dwarfs a small-scale (~ 8 kpc) double source at the center of NGC 1407. Based on former *GMRT* observations, G11 suggested that the diffuse outer emission was produced during an earlier cycle of activity of NGC 1407. The spectral analysis presented in this paper corroborates the multiple outburst scenario. The large-scale emission is found to have an ultra-steep radio spectrum, with $\alpha = 1.82$, as typically observed for highly evolved and fading radio sources (e.g., Komissarov & Gubanov 1994; Parma et al. 2007; Giacintucci et al. 2007; Murgia et al. 2011). The spectral age analysis suggests that the radio plasma in such component is at least ~ 300 Myr old. Furthermore, the radiative model that better describes the spectrum of this emission requires a switch-off of the nuclear engine ~ 170 – 190 Myr ago, followed by a dying phase. The inner double has instead a spectral index of $\alpha = 0.7$ and a radiative age of ~ 30 Myr, consistently with being a currently active and relatively young radio source.

The multi-scale radio morphology, combined with the distinct spectral properties of its components, makes NGC 1407 another remarkable example of a *nesting* radio galaxy, other nearby examples being, for instance, 4C29.30 (Jamrozy et al. 2007) and Hercules A (Gizani et al. 2005). As double-double radio galaxies, these peculiar radio sources provide evidence for recurrent radio activity in elliptical galaxies. In the specific case of NGC 1407, the small, young double source is currently fed by the central AGN, while the diffuse, steep-spectrum component is associated with relic plasma, which was injected during an earlier radio outburst of the AGN occurred at least ~ 300 Myr ago.

It is important to note that our radiative ages have been estimated neglecting adiabatic expansion. This could be a reasonable approximation for a relaxed, aged plasma in the dying phase such as that in the large-scale component. However, expansion losses can be important for the inner double, as well as for the earlier, active phase of the large-scale component. Indeed, neglecting their effect may lead to an underestimate

of the true source age.

Our age derivation is also based on the assumption of uniform and constant magnetic field across the source. A calculation of the effects of magnetic field evolution is beyond the purpose of the present paper, and we refer to Rudnick et al. (1994), Jones et al. (1999), Blundell & Rawlings (2000), and references therein, for detailed works on the implications of magnetic field evolution for the source aging. In the case of very aged emission as that in NGC 1407, the relativistic plasma may be partially mixed with the hot thermal gas. In this case, magnetized filaments can be produced in the radio volume due to plasma instabilities and the total synchrotron emission would result from the convolution of different spectra produced by relativistic electrons emitting in regions with different magnetic field strength (e.g., Tregillis et al. 2004). The resulting convolution of the synchrotron kernel with magnetic field intensity and geometry yields a total spectrum which is stretched and thus not straightforwardly related to the spectrum of the emitting electrons (e.g., Eilek & Arendt 1996; Katz-Stone & Rudnick 1997). In this case, standard aging analyses, based on the position of the break frequency in the synchrotron spectrum, can give incorrect estimates of the age of the radio emitting electrons.

7.2. Energy output of the radio outbursts

We compared the energy output associated with synchrotron radiation from the two radio outbursts in NGC 1407. Using the radio luminosity at 240 MHz and α_{inj} in Table 5, we calculated the total radio luminosity over the frequency range 10 MHz–100 GHz adopting the expression in O’Dea & Owen (1987). We found a bolometric radiative power of $L_{\text{tot}} \sim 1.6 \times 10^{42}$ erg s^{-1} for the inner double and $L_{\text{tot}} \sim 3.2 \times 10^{42}$ erg s^{-1} for the large-scale emission. Based on our estimates of the radiative age of the two components (Table 5), we found that the current outburst has released an energy of $E_{\text{tot, syn}} \sim 1.5 \times 10^{57}$ erg so far, while the energy of the former episode of activity, $E_{\text{tot, syn}} \sim 2.6$ – 3.2×10^{58} erg, is one order of magnitude larger.

It is well known that the synchrotron luminosity is an underestimate of the total energy output of a radio source, which is believed to be dominated by the mechanical work done by the radio jets on the external medium. The mechanical jet power of radio sources can be inferred, for instance, in those groups/clusters with depressions (cavities) in their X-ray surface brightness, interpreted as rising bubbles of relativistic plasma inflated by the central AGN (e.g., Bîrzan et al. 2004, 2008; Cavagnolo et al. 2010; O’Sullivan et al. 2011). Here, it is estimated that the ratio of the mechanical to synchrotron luminosities is a few to few thousands for powerful radio sources, and up to several thousand for weaker sources (e.g., Bîrzan et al. 2004). In those special systems with multiple cavities, interpreted as signature of repeated AGN outbursts, it is also possible to compare the energy outputs of the different episodes of activity. In some systems, such as Hydra A (Wise et al. 2007) and NGC 5813 (Randall et al. 2011), it is found that the past epoch of activity is the most energetic, suggesting that the mean jet power changed significantly over time or that the current outburst is still ongoing. In other systems (e.g., A 262, Clarke et al. (2009)), there is evidence for an opposite outburst trend, which may reflect an increase of the fueling of the AGN with time.

The current X-ray images of NGC 1407 do not show evidence of X-ray cavities associated with the large-scale diffuse

radio structure. Dong et al. (2010) report a possible small (0.7×0.4 kpc) cavity in the group core, but its identification is dependent on the image processing employed and it appears to be uncorrelated with the small-scale active radio source. A direct measurement of the mechanical power of the radio jets in either period of activity is therefore not possible. If the mean jet mechanical power to radio power ratio has remained constant over the outburst history, NGC 1407 would then be another system in which the total energy output from the AGN is decreasing with time. On the other hand, the most recent episode of activity may be still ongoing (its radiative age is ~ 30 Myr), and it is possible that the jet power may increase.

7.3. Pressure comparison

Assuming energy equipartition arguments, we can derive the non-thermal pressure in the radio source and compare it to the pressure of the surrounding X-ray gas. Under the assumptions listed at the beginning of Sect. 4 (see point 3), and adopting α_{inj} and B_{eq} in Table 5, we calculated a radio pressure in the large-scale component of $P_{\text{radio,diffuse}} = 2.5 \times 10^{-13}$ erg cm $^{-3}$ and $P_{\text{radio,S3}} = 2.8 \times 10^{-12}$ erg cm $^{-3}$ for the inner double.

Even though the X-ray pressure profile in Fig. 11 does not cover the whole extent of the radio emission, it is clear that the pressure of the X-ray gas is at least one order of magnitude higher than the radio pressure, with values ranging from $\sim 10^{-11}$ erg cm $^{-3}$ at ~ 10 kpc from the center to $\sim 5 \times 10^{-12}$ erg cm $^{-3}$ at ~ 40 kpc. This is not unusual for cool-core systems, where a similar pressure discrepancy is often found (e.g., Dunn et al. 2005), suggesting a departure from equipartition conditions or an additional pressure support in the radio lobes, for instance, in the form of thermal gas (e.g., O’Sullivan et al. 2010). Alternatively, an energetically dominant population of non-radiating relativistic particles (protons) may contribute to the internal pressure. The achievement of pressure balance in NGC 1407 would then require a ratio of energy in non-radiating particles to the energy in electrons $k \sim 100 - 1000$. These values are in the range typically found for samples of centrally-located radio galaxies in groups and clusters (Dunn & Fabian 2004; Bîrzan et al. 2008; Croston et al. 2008; Gitti et al. 2010) and suggest that the lobes have been fed by *heavy* jets or have entrained thermal material during their propagation through the cluster/group atmosphere (e.g., O’Sullivan et al. 2010). The diffuse and distorted morphology of the large-scale emission in NGC 1407, combined with the very long age inferred for this component, suggest that a mixing of the radio plasma and ambient thermal gas has already occurred at some level, favoring the entrainment scenario.

7.4. Motion of the galaxy

The morphology of NGC 1407 in the X-ray band (Fig. 8 and Fig.9) suggests that the galaxy is in motion. A surface brightness edge is visible in the north side of the galaxy with gas swept back to the east and west into two cool wings. There is some indication of a possible discontinuity in the surface brightness profile of the northern quadrant of the galaxy at this position (Fig. 10). If confirmed, this feature would suggest the presence of a shock or a cold front. The Fe-peak temperature map shows variations across the edge which seem consistent with the hypothesis of a cold front, i.e., with the cooler gas behind the front (Fig. 12). However, the available data are not deep enough to constrain the temperature jump across the

edge and thus the nature of this feature.

Overall, NGC 1407 appears to be moving northward with its halo being stripped by the surrounding IGM. The location of the putative front is consistent with this scenario. If the edge is a cold front, it may indicate that the gas is sloshing in response to a recent interaction, such as a close passage, of NGC 1400. The X-ray trail visible in the *XMM* image (Fig. 8) could originate from the same interaction.

The diffuse radio structure also shows a swept-back shape, but on a larger scale, similar to wide-angle tail (WAT) radio galaxies, although no jets are present. As discussed above, this emission is found to be the remnant of a former radio outburst of the central galaxy, consistent with the absence of jets. The X-ray wings seem to be inside the radio emission, and the radio contours appear compressed at the northern edge (e.g., Fig. 12).

The similarities in the radio and X-ray morphologies suggest that the two structures are co-spatial and both affected by the motion of the galaxy. The X-ray wings may then represent a wake of cooler galactic material which has been stripped by the same ram-pressure that bent the diffuse radio emission.

There are several ways in which we can obtain rough estimates of the velocity of NGC 1407 relative to the IGM. If we assume, for simplicity, that the bending of the diffuse radio emission is caused by ram pressure, we can use the Euler equation in the form

$$\frac{\rho_{\text{radio}} v_{\text{radio}}^2}{r_c} = \frac{\rho_{\text{IGM}} v_{\text{gal}}^2}{r_{\text{radio}}}$$

(e.g., O’Dea 1985), where r_c is their curvature radius, r_{radio} is the radius of the radio *tails*, ρ_{radio} and v_{radio} are the density and velocity of the radio-emitting plasma, v_{gal} is the velocity of the galaxy relative to the IGM, and ρ_{IGM} is the density of the IGM. From the images presented in Sect. 3, we estimate $r_{\text{radio}} \sim 10$ kpc and $r_c \sim 30$ kpc. Based on the spatial extent of the diffuse radio emission ($\text{LLS} \sim 80$ kpc) and age of the active phase $t_{\text{CI}} \sim 90 - 130$ Myr (Table 5), we derive a first order estimate of the growth velocity of the radio source of $v_{\text{radio}} = \text{LLS}/t_{\text{CI}} \sim 0.002c - 0.003c$, where c is the speed of light. Finally, from the *Chandra* data, we obtain $\rho_{\text{IGM}} \sim 0.0015$ cm $^{-3}$ within the central 50 kpc and assume $\rho_{\text{radio}} \sim 10^{-3} \rho_{\text{IGM}}$ (e.g., Douglass et al. 2011). This gives a very low velocity, only $v_{\text{gal}} \sim 20$ km s $^{-1}$.

Alternatively, we can make a simple calculation assuming that the galaxy is moving north, that the radio outburst was located where we now see the southern boundary of the diffuse structure, and that it has moved at a constant velocity since that time. Neglecting projection effects and basing our estimate on the 240 MHz map, the galaxy would then have traveled 28-35 kpc over a period of ~ 300 Myr, suggesting a velocity of 90-115 km s $^{-1}$.

These velocity estimates conflict to some extent with the X-ray morphology. If a cold front is present in NGC 1407, we would expect the galaxy to be moving at a significant fraction of the sound speed. For a temperature of 1.1 keV, as is found immediately north of the surface brightness edge, the sound speed is $v_{\text{sonic}} \sim 500$ km s $^{-1}$, so a velocity of at least 250 km s $^{-1}$ would be likely.

However, there are large uncertainties on our estimates. If sloshing is taking place, the most likely cause is perturbation by a tidal encounter with NGC 1400. Given the 1100 km s $^{-1}$ velocity offset between NGC 1400 and the group mean, it is

clear that sloshing motions would include a significant line of sight component. Since we see signs of a surface brightness edge in the X-ray and compressed contours in the radio, the velocity in the plane of the sky is greater than or comparable to that in the line of sight, but this still leaves an uncertainty of up to a factor $\sqrt{2}$ in the true velocity of NGC 1407. The velocity could thus be as high as 160 km s^{-1} , or $0.3v_{\text{sonic}}$.

Projection effects could have an impact on our estimate of the ram-pressure timescale. If the diffuse structure is in fact two old radio lobes, the axis of the jet which formed them may have been at an angle to the line of sight. In this case the lobes would be at a larger radius than we have assumed, and would experience lower external pressures. Mixing of entrained thermal plasma into the lobes would raise their effective density. Both of these factors could increase the ram-pressure velocity estimate, though it is difficult to place limits on their impact.

As discussed above, the X-ray images of NGC 1407 suggest that the group is not relaxed. A connection between bending of radio jets and sloshing induced by minor mergers has been proposed in cluster cores (e.g., Clarke et al. 2004; Ascasibar & Markevitch 2006; Mendygral et al. 2012), and it seems possible that NGC 1407 is an example of this process at work in a galaxy group. In particular, we speculate that the group core is sloshing along the North-South axis, in response to a possible recent interaction with the nearby group galaxy NGC 1400. The gas motions induced by such sloshing may be then shaping both the X-ray and radio structures. There is a degree of tension between the velocities estimated from the radio and X-ray data. Resolving this issue would require deeper X-ray data, capable of detecting any cold front and providing a more reliable velocity measurement, and of determining the filling factor of the diffuse radio structure.

8. SUMMARY

We have examined the complex radio emission associated with the galaxy NGC 1407, at the center of the group Eridanus A. In a previous work, we have suggested that the galaxy experienced two distinct radio outbursts. Thanks to new, deep *GMRT* observations at 240 MHz, 330 MHz and 610 MHz, combined with archival *VLA* data, we confirm the multiple-outburst scenario. NGC 1407 appears to be currently active in the radio band in the form of a small-scale ($\sim 8 \text{ kpc}$) double source associated with the galaxy. The analysis of the integrated radio spectrum indicates that the source has a spectral index of 0.7 and a radiative age of $\sim 30 \text{ Myr}$, consistent with being an active and relatively young radio source. The double is wholly embedded in a faint, diffuse component, extending on a scale which is almost an order of magnitude larger ($\sim 80 \text{ kpc}$). The large-scale emission is found to have an ultra-steep spectrum, with $\alpha = 1.8$, as typically found for highly evolved and/or dying radio galaxies. The spectral age analysis shows that the radio plasma in such a component is at least $\sim 300 \text{ Myr}$ old, supporting the idea that it was generated during a former radio outburst of NGC 1047. We estimated that the radio nucleus switched off $\sim 170\text{--}190 \text{ Myr}$ ago, and after this time the source entered a dying phase.

We compared the synchrotron energy output associated with the two radio outbursts and found that the energy released during the duration of its current activity is nearly an order of magnitude lower than that from the former outburst. Numerous studies in the literature have shown that the synchrotron luminosity is an underestimate of the total energy

output of a radio source, which is dominated by the mechanical work done by the jets on the external medium. If the mean jet power remained constant over the whole outburst history of NGC 1407, then NGC 1407 would be another example of a system in which the energy output is decreasing with time, other examples being Hydra A and NGC 5813. On the other hand, the most recent episode of activity may be still ongoing, and it is possible that the jet power may increase.

We analyzed *XMM-Newton* and *Chandra* observations of the group. The diffuse emission surrounding NGC 1407 appears swept back to the south, with wings extending to the east and west, and a possible surface brightness discontinuity on the northern side of the galaxy. Temperature mapping shows the emission inside the edge to be cooler than that to the north, but the data are shallow and the smoothing scale is too large to confirm whether a cold front or weak shock is present. The northern edge coincides with regions of compressed radio contours, and the large-scale radio structure also has a swept-back morphology, indicating that the radio and X-ray structures are co-spatial and affected by the same forces. In general, the radio and X-ray morphology are suggestive of northward motion. We speculate that the group core may be sloshing on a north-south axis within the larger group potential, having been tidally disturbed by an encounter with the nearby elliptical NGC 1400. Our estimated velocity in the plane of the sky is relatively low ($\sim 100 \text{ km s}^{-1}$), but given the large uncertainties it seems possible that the true velocity could be a significant fraction of the sound speed, in which case sloshing motions could produce the radio and X-ray features we observe.

Comparison of pressure estimates for the large-scale radio structure and the surrounding intra-group medium show the usual order-of-magnitude difference, the X-ray pressure estimate being much higher than that found from the radio data. This may indicate a large population of non-radiating particles within the radio structure, with a total energy $\sim 100\text{--}1000$ times that of the relativistic electron population. If, as seems likely, the structure was formed by a previous AGN outburst, these particles could be relativistic protons accelerated within the original radio jets, or a thermal plasma component which has been entrained during the propagation and expansion of the jets and lobes. The latter possibility provides an explanation for the continued presence of the radio structure in the group core, since buoyant forces, which would normally lift the lobes into the outskirts of the group halo, will be suppressed if the lobes contain a large fraction of thermal plasma.

We thank the staff of the GMRT for their help during the observations. GMRT is run by the National Centre for Radio Astrophysics of the Tata Institute of Fundamental Research. SG acknowledges the support of NASA through Einstein Postdoctoral Fellowship PF0-110071 awarded by the *Chandra* X-ray Center (CXC), which is operated by the Smithsonian Astrophysical Observatory (SAO). EOS acknowledges the support of the European Community under the Marie Curie Research Training Network. Basic research in astronomy at the Naval Research Laboratory is funded by 6.1 Base funding. JMV, LPD and EOS acknowledges the support of the Smithsonian Institution and CXC. The National Radio Astronomy Observatory is a facility of the National Science Foundation operated under cooperative agreement by Associated Universities, Inc. This research has made use of the NASA/IPAC Extragalactic Database (NED) which is operated by the Jet

Propulsion Laboratory, California Institute of Technology, un-

der contract with the National Aeronautics and Space Administration.

REFERENCES

- Ascasibar, Y., & Markevitch, M. 2006, *ApJ*, 650, 102
- Baars, J. W. M., Genzel, R., Pauliny-Toth, I. I. K., & Witzel, A. 1977, *A&A*, 61, 99
- Beck, R., & Krause, M. 2005, *Astronomische Nachrichten*, 326, 414
- Birzan, L., Rafferty, D. A., McNamara, B. R., Wise, M. W., & Nulsen, P. E. J. 2004, *ApJ*, 607, 800
- Birzan, L., McNamara, B. R., Nulsen, P. E. J., Carilli, C. L., & Wise, M. W. 2008, *ApJ*, 686, 859
- Blundell, K. M., & Rawlings, S. 2000, *AJ*, 119, 1111
- Brough, S., Forbes, D. A., Kilborn, V. A., Couch, W., & Colless, M. 2006, *MNRAS*, 369, 1351
- Brunetti, G., Setti, G., & Comastri, A. 1997, *A&A*, 325, 898
- Burns, J. O., Rhee, G., Owen, F. N., & Pinkney, J. 1994, *ApJ*, 423, 94
- Cavagnolo, K. W., McNamara, B. R., Nulsen, P. E. J., et al. 2010, *ApJ*, 720, 1066
- Chandra, P., Ray, A., & Bhatnagar, S. 2004, *ApJ*, 612, 974
- Clarke, T. E., Blanton, E. L., & Sarazin, C. L. 2004, *ApJ*, 616, 178
- Clarke, T. E., Ensslin, T. A. 2006, *AJ*, 131, 2900
- Clarke, T. E., Blanton, E. L., Sarazin, C. L., et al. 2009, *ApJ*, 697, 1481
- Cohen, A. S., Lane, W. M., Cotton, W. D., Kassim, N. E., Lazio, T. J. W., Perley, R. A., Condon, J. J., & Erickson, W. C. 2007, *AJ*, 134, 1245
- Condon, J. J., Cotton, W. D., Greisen, E. W., et al. 1998, *AJ*, 115, 1693
- Croston, J. H., Hardcastle, M. J., Birkinshaw, M., Worrall, D. M., & Laing, R. A. 2008, *MNRAS*, 386, 1709
- David, L. P., Jones, C., Forman, W., et al. 2009, *ApJ*, 705, 624
- De Vaucouleurs, G., De Vaucouleurs, A., Corwin Jr., H. G., Buta, R. J., Paturel, G., Fouque, P., Third Reference Catalogue of Bright Galaxies, Version 3.9
- Diehl, S., & Statler, T. S. 2008, *ApJ*, 687, 986
- Dong, R., Rasmussen, J., & Mulchaey, J. S. 2010, *ApJ*, 712, 883
- Douglass, E. M., Blanton, E. L., Clarke, T. E., Randall, S. W., & Wing, J. D. 2011, *ApJ*, 743, 199
- Dunn, R. J. H., & Fabian, A. C. 2004, *MNRAS*, 355, 862
- Dunn, R. J. H., Fabian, A. C., & Taylor, G. B. 2005, *MNRAS*, 364, 1343
- Eilek, J. A., Burns, J. O., O'Dea, C. P., & Owen, F. N. 1984, *ApJ*, 278, 37
- Eilek, J. A., & Arendt, P. N. 1996, *ApJ*, 457, 150
- Forbes, D. A., Ponman, T., Pearce, F., et al. 2006, *PASA*, 23, 38
- Giacintucci, S., Venturi, T., Murgia, M., et al. 2007, *A&A*, 476, 99
- Giacintucci, S., Venturi, T., Macario, G., et al. 2008, *A&A*, 486, 347
- Giacintucci, S., et al. 2011, *ApJ*, 732, 95 (G11)
- Gizani, N. A. B., & Leahy, J. P. 2003, *MNRAS*, 342, 399
- Gitti, M., O'Sullivan, E., Giacintucci, S., et al. 2010, *ApJ*, 714, 758
- Gizani, N. A. B., Cohen, A., & Kassim, N. E. 2005, *MNRAS*, 358, 1061
- Gomez, P. L., Pinkney, J., Burns, J. O., et al. 1997, *ApJ*, 474, 580
- Grevesse, N., & Sauval, A. J. 1998, *Space Sci. Rev.*, 85, 161
- Greisen, Eric W., Spekkens, Kristine, van Moorsel, Gustaaf A. 2009, *AJ*, 137, 4718
- Jaffe, W. J., & Perola, G. C. 1973, *A&A*, 26, 423
- Jamrozny, M., Konar, C., Saikia, D. J., Stawarz, L., Mack, K.-H., & Siemiginowska, A. 2007, *MNRAS*, 378, 581
- Jansen, F., Lumb, D., Altieri, B., et al. 2001, *A&A*, 365, L1
- Jones, T. W., Ryu, D., & Engel, A. 1999, *ApJ*, 512, 105
- Kardashev, N. S. 1962, *Soviet Ast.*, 6, 317
- Katz-Stone, D. M., & Rudnick, L. 1997, *ApJ*, 488, 146
- Komissarov, S. S., & Gubanov, A. G. 1994, *A&A*, 285, 27
- Lara, L., Márquez, I., Cotton, W. D., Feretti, L., Giovannini, G., Marcaide, J. M., & Venturi, T. 1999, *A&A*, 348, 699
- Leahy, J. P., Pooley, G. G., & Riley, J. M. 1986, *MNRAS*, 222, 753
- Mendygral, P., Jones, T., & Dolag, K. 2012, arXiv:1203.2312
- Myers, S. T., & Spangler, S. R. 1985, *ApJ*, 291, 52
- Mulchaey, J. S., Davis, D. S., Mushotzky, R. F., & Burstein, D. 2003, *ApJS*, 145, 39
- Murgia, M., et al. 2011, *A&A*, 526, A148
- O'Dea, C. P. 1985, *ApJ*, 295, 80
- O'Dea, C. P., & Owen, F. N. 1987, *ApJ*, 316, 95
- O'Donoghue, A. A., Eilek, J. A., & Owen, F. N. 1993, *ApJ*, 408, 428
- O'Sullivan, E., Vrtilik, J. M., Harris, D. E., & Ponman, T. J. 2007, *ApJ*, 658, 299
- O'Sullivan, E., Giacintucci, S., Vrtilik, J. M., Raychaudhury, S., & David, L. P. 2009, *ApJ*, 701, 1560
- O'Sullivan, E., Giacintucci, S., David, L. P., Vrtilik, J. M., & Raychaudhury, S. 2010, *MNRAS*, 407, 321
- O'Sullivan, E., Worrall, D. M., Birkinshaw, M., et al. 2011, *MNRAS*, 416, 2916
- Pacholczyk, A. G. 1970, *Series of Books in Astronomy and Astrophysics*, San Francisco: Freeman, 1970
- Parma, P., Murgia, M., de Ruiter, H. R., et al. 2007, *A&A*, 470, 875
- Quintana, H., Fouque, P., & Way, M. J. 1994, *A&A*, 283, 722
- Randall, S. W., Forman, W. R., Giacintucci, S., et al. 2011, *ApJ*, 726, 86
- Rasmussen, J., & Ponman, T. J. 2007, *MNRAS*, 380, 1554
- Roettiger, K., Burns, J. O., & Loken, C. 1996, *ApJ*, 473, 651
- Rudnick, L., Katz-Stone, D. M., & Anderson, M. C. 1994, *ApJS*, 90, 955
- Saikia, D. J., Konar, C., & Kulkarni, V. K. 2006, *MNRAS*, 366, 1391
- Saikia, D. J., & Jamrozny, M. 2009, *Bulletin of the Astronomical Society of India*, 37, 63
- Schoenmakers, A. P., de Bruyn, A. G., Röttgering, H. J. A., van der Laan, H., & Kaiser, C. R. 2000, *MNRAS*, 315, 371
- Subrahmanyan, R., Saripalli, L., & Hunstead, R. W. 1996, *MNRAS*, 279, 257
- Tregillis, I. L., Jones, T. W., & Ryu, D. 2004, *ApJ*, 601, 778
- Trentham, N., Tully, R. B., Mahdavi, A. 2006, *MNRAS*, 369, 1375
- van Breugel, W., & Fomalont, E. B. 1984, *ApJ*, 282, L55
- Weisskopf, M. C., Brinkman, B., Canizares, C., et al. 2002, *PASP*, 114, 1
- Wise, M. W., McNamara, B. R., Nulsen, P. E. J., Houck, J. C., & David, L. P. 2007, *ApJ*, 659, 1153